applied sciences

MDPI

Article

Characterizing Internal Flow Field in Binary Solution Droplet Combustion with Micro-Particle Image Velocimetry

Bingyao Huang, Haodong Zhang, Zundi Liu, Xiaoyuan Yang, Wei Li and Yuyang Li *

Institute of Aerospace Propulsion, School of Mechanical Engineering, Shanghai Jiao Tong University, Shanghai 200240, China; huangby@sjtu.edu.cn (B.H.); zhanghd2020@outlook.com (H.Z.); zundiliu@sjtu.edu.cn (Z.L.); yangxy17@sjtu.edu.cn (X.Y.); lw2017@sjtu.edu.cn (W.L.)
* Correspondence: yuygli@sjtu.edu.cn

Featured Application: This paper investigates the internal flow fields in suspended binary solution droplets during combustion and discusses the influence of flow velocity on mass transfer and content gradient formation in the binary droplets.

Abstract: Droplet internal flow participates in liquid-phase mass transfer during multicomponent solution droplet combustion. In this work, internal flow fields in the binary droplet combustion of two polyoxymethylene dimethyl ethers ($CH_3O(CH_2O)_nCH_3$, $n \geq 1$, abbreviated as $PODE_n$), i.e., $PODE_2$ and $PODE_4$, are characterized using micro-particle image velocimetry (Micro-PIV). The buoyancy-driven upward vapor flow around the droplet is found to initiate two opposite radial flows in the droplet, which form two vortex cores near the surface, while the gravitational effect and Marangoni effect resulting from the content and temperature gradients in the binary droplets can induce disturbance to the two flows. The binary droplets have comparable spatially averaged flow velocities at the stable evaporation stage to those of pure droplets, which are around 3 mm/s. The velocity curves are more fluctuant and tend to slightly increase and reach the peak values at around 250 ms, and then decrease until droplet atomization. The flow velocities in the droplet interior are generally higher than those near the droplet surface, forming a parabolic velocity profile along the horizontal radial direction. The peak velocity first increases to 5–9 mm/s as the radial flow and vortex structure start to form and then decreases to around 3 mm/s until droplet atomization. The radial flow with a spatially averaged velocity of 3 mm/s can run around one lap during the stable evaporation stage, which implies that the convection-induced mass transfer is relatively weak, and consequently, the content gradient of the binary droplet is still mainly controlled by mass diffusion.

Keywords: $PODE_n$; droplet combustion; internal flow field; micro-PIV; mass transfer

check for updates

Citation: Huang, B.; Zhang, H.; Liu, Z.; Yang, X.; Li, W.; Li, Y. Characterizing Internal Flow Field in Binary Solution Droplet Combustion with Micro-Particle Image Velocimetry. *Appl. Sci.* **2023**, *13*, 5752. https://doi.org/10.3390/app13095752

Academic Editor: Roberto Camussi

Received: 29 March 2023
Revised: 28 April 2023
Accepted: 4 May 2023
Published: 6 May 2023

Copyright: © 2023 by the authors. Licensee MDPI, Basel, Switzerland. This article is an open access article distributed under the terms and conditions of the Creative Commons Attribution (CC BY) license (https://creativecommons.org/licenses/by/4.0/).

1. Introduction

The droplet evaporation process is a common phenomenon around us and has attracted great attention because of its wide applications in various technologies such as spray combustion [1], spray drying [2], and medical diagnostics [3]. Understanding the internal flow in the evaporating droplet is important for a better understanding of the evaporation and atomization mechanisms. Take the classical "coffee stain problem" as an example. When a spilled drop of coffee dries on a solid surface, it leaves a dense, ring-like deposit along the perimeter. The coffee ring pattern was found to be caused by the capillary flow, which can carry almost all the solid materials from the droplet interior to the droplet edge. This phenomenon is common for any droplet containing dispersed particles evaporating on a solid surface [4]. The discovery of an internal capillary flow in a slurry droplet has brought great improvement for some applications like surface coating [5] and inkjet printing [6]. For a multicomponent solution droplet, especially during combustion, the highly volatile components evaporate faster than the weakly volatile components on the droplet surface,

which can result in content gradient in the droplet and make the multicomponent droplet undergo a violent atomization process [7]. Internal flow in the multicomponent solution droplet can influence the mass transfer process and, thus, influence the content gradient in the droplet, which is important in studying multicomponent droplet evaporation and atomization during combustion [8,9].

Previous studies about the internal flow in multicomponent droplets focused on sessile or pendant droplets which are in direct contact with the substrate or Leidenfrost droplets floating on a substrate [10–16]. Li et al. [15] studied the gravitational effect in evaporating binary droplets with a small Bound number. They measured the flow fields near the substrate by micro-PIV for both the sessile droplets and pendant droplets during the evaporation process and observed two opposite radial flows in the droplets. They found that the directions of the two opposite radial flows are the same in both sessile droplets and pendant droplets; thus, they concluded that these flow patterns are caused by the gravitational effect that is induced by the content gradient in the droplets. However, the content gradient will induce not only the gravitational effect but also the Marangoni effect. Therefore, they also performed another numerical study on the competing Rayleigh flow induced by the gravitational effect and Marangoni flow in binary droplet evaporation [12]. They proposed a quasi-stationary model for the internal flows in sessile or pendant binary droplets based on the Rayleigh number and Marangoni number, which successfully predicted the competition and interaction between the Rayleigh flow and Marangoni flow. The content gradient and temperature gradient were concluded to be the main factors of the Rayleigh flow and Marangoni flow in the sessile or pendant droplets [11–15].

For Leidenfrost droplets, the vapor around the droplet flows upward because of the buoyancy effect and can induce internal flow for both multicomponent droplets and pure droplets. Bouillant et al. [10] studied the flow field in rolling Leidenfrost droplets called the Leidenfrost wheels. They found that the vapor flow around the droplet can induce a rapid internal flow accompanied by a tilting of the droplet base, which creates a permanent ratchet-like mechanism for the rolling of the droplet. Lyu et al. [16] studied the internal flow in an explosive boiling multicomponent Leidenfrost droplet. They found two large vortices in the cross-section of the droplet that belong to a toroidal vortex. They concluded that the viscous flow in the vapor layer from the base of the droplet to the periphery contributes to this internal flow regime, i.e., moving upward near the droplet surface and downward in the droplet center. Although the temperature gradient and content gradient can cause Marangoni flow in the droplet, the measured results revealed that it is relatively weaker than the vapor-induced flow. These studies show that the vapor flow around the Leidenfrost droplet is usually the main factor to induce the internal flow in the droplet.

In practical spray combustion process, droplets are dominantly burnt under the unconstrained environment. Different from sessile droplets and Leidenfrost droplets, which are strongly affected by the solid surface, droplets suspended on fibers are much closer to the combustion condition. Previous studies about internal flow in droplets suspended on fibers are limited [17–19]. Antonov et al. [17] studied the flow field in the suspended water/oil droplet with the upward vapor flow. They found that the values of flow velocities in the aqueous phase and oil phase are rather different, while the velocities both show increasing trends as the temperature of upward vapor flow increases. He et al. [18] studied the internal flow fields in aviation kerosene droplets during combustion. They used the soot particles in the droplet as tracers to visualize the fluid motion in the droplet and also observed the dual-vortices flow field structure in the cross-section of the droplet originated from a toroidal vortex. They concluded that the Marangoni effect caused by the temperature gradient on the droplet surface is the main reason for the observed flow field structure. On the other hand, Mandal et al. [19] proposed that both thermal Marangoni effect and solutal Marangoni effect exist during the evaporation of multicomponent droplets. They put the droplet in a closed chamber to avoid any surrounding disturbance and observed an oscillating convection inside the droplet that was attributed to the competition between the thermal Marangoni effect and solutal Marangoni effect. It is obvious that these studies

usually did not consider all the factors that can influence the internal flow, especially the upward vapor flow during combustion and the gravitational effect caused by the content gradient. In particular, previous studies did not pay attention to the influence of internal flow on the mass transfer process and content gradient formation during the combustion of multicomponent droplets. Therefore, more studies are desired for a deep understanding of the internal flow in a suspended multicomponent droplet during combustion.

In this work, micro-PIV is used to measure the internal flow fields in suspended binary solution droplets during combustion. Two $PODE_n$ components, which are among the major e-fuel families and have been recognized as promising alternative fuels and additives for combustion engines [20], i.e., $PODE_2$ and $PODE_4$, are used as the highly volatile component and weakly volatile component, respectively. The influential factors for the internal flow field structures are revealed. The spatially averaged flow velocity evolution and the velocity distribution in the flow field at the stable evaporation stage are derived. The influence of internal flow on the mass transfer process and content gradient formation in the binary droplets is also analyzed and discussed.

2. Materials and Methods

The droplet combustion apparatus used in this work is shown in Figure 1, which is the same as that used in our previous work [7]. Therefore, only a brief introduction is provided here. Two quartz fibers with the diameter of 100 μm were crossed to suspend the droplet. The diameters of the initially suspended droplets were maintained at 1.2–1.6 mm, which is over an order of magnitude thicker than the fiber diameter. During each experiment, the droplet was ignited by an electric spark generated by two electrodes that were synchronized with a high-speed camera (Phantom VEO1310L). The ignition energy was controlled at 100 mJ, and the ignition duration time was set as 100 ms in all experiments. An acrylic chamber was used to avoid disturbance from any surrounding airflow. The pressure, temperature, and relative humidity in the chamber are 1 atm, 25 °C, and 25%, respectively. During the experiment, the droplet is surrounded by a flame.

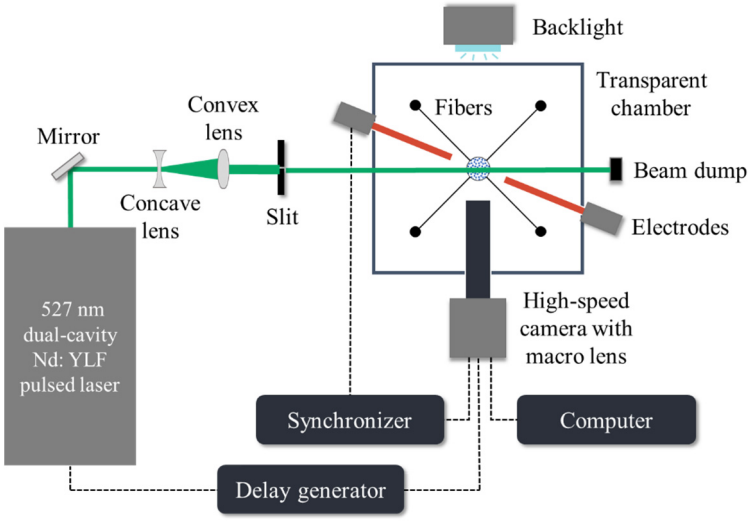


Figure 1. Schematic diagram of the droplet combustion apparatus combined with a micro-PIV system.

TiO_2 particles with diameters around 1 μm were seeded in the binary droplets. The droplets were sonicated to ensure uniform dispersion of the tracer particles. In the micro-PIV system, a high-speed camera (Phantom VEO 1310L) and a 527 nm dual-cavity Nd:YLF pulsed laser (Beamtech Optronics, Vilte-Hi-527-40) were operated at 800 Hz and synchronized by a LabVIEW delay generator program based on a digital I/O module (NI PCIe-7856). Tracer particles in the droplets were illuminated through the thin laser sheet. The video of the droplet combustion constituted by particle images was recorded by the high-speed camera operated in dual mode with a macro lens (Navitar Zoom 6000) attached

with a short bandpass filter (Edmund Optics 527/20 nm). The time interval of two consecutive frames can be regulated. The field of view of this camera was set as 80 mm × 60 mm, corresponding to a spatial resolution of ~3 µm/pixel. The frame rate was set as 800 fps, and the maximum recorded duration was set as 3 s to capture the whole lifetime of the droplet.

The data processing procedure of particle images is shown in Figure 2. All steps were accomplished with DaVis 8.4 and MATLAB. First, the raw particle image was calibrated and scaled to the global coordinate system. Second, the image was preprocessed and a sliding background was subtracted from the particle image to reduce the fluctuation of background intensity. Then, an algorithm mask based on a count threshold was applied to separate the target domain from the whole image. Subsequently, a multi-pass cross-correlation algorithm was applied to calculate the velocity vectors and some basic post-processing operations were used to remove obviously erroneous velocity vectors. Therefore, the flow field inside a binary droplet can be acquired, which has the velocity field overlapped with vector arrows and the vorticity field overlapped with streamlines. Using a statistical analysis of how each pixel contributes to the cross-correlation peak shape, the uncertainty of the velocity field is derived [21]. For the following results in this work, the maximum uncertainty of the velocity is 0.2 mm/s.

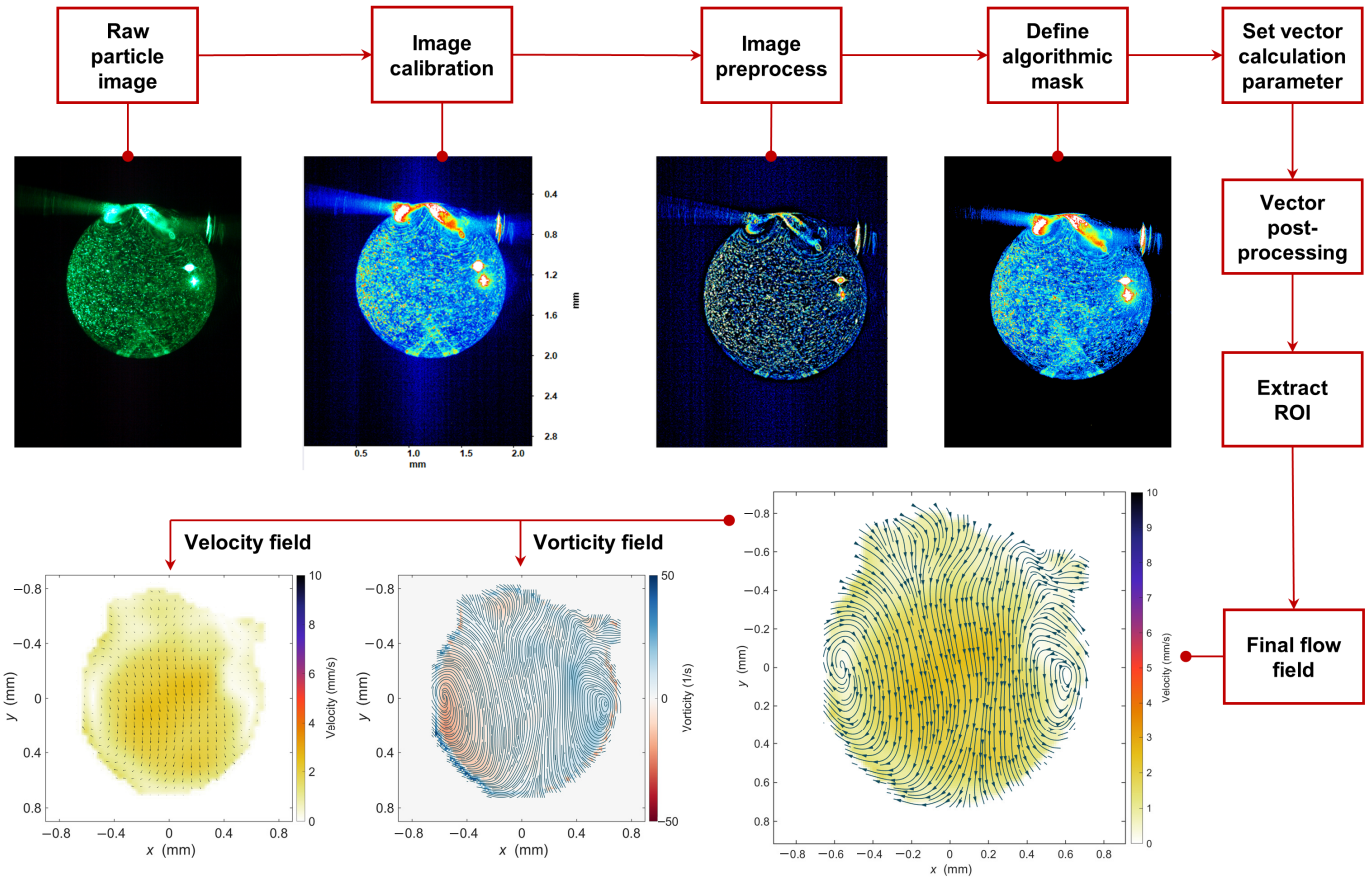


Figure 2. Data processing procedure from raw particle image to flow field.

In this work, the two fuel components, i.e., $PODE_2$ and $PODE_4$, are mixed at different content ratios (volume fractions). Table 1 lists the composition, content ratios, boiling point difference (ΔT_{bp}), and nomenclatures of the investigated binary solution droplets in this work. The two components are perfectly miscible, and the binary mixtures have been ultrasonicated for at least 30 min. Therefore, the binary droplets are uniformly mixed. For better comparison, pure $PODE_2$ and $PODE_4$ droplets are also investigated.

Table 1. A list of the investigated binary solution droplets in this work, along with their content ratios, ΔT_{bp}, and nomenclatures.

Composition	Content Ratio	ΔT_{bp} (K)	Nomenclature
$PODE_2/PODE_4$	10%/90%	97	10P2/90P4
	30%/70%		30P2/70P4
	50%/50%		50P2/50P4
	70%/30%		70P2/30P4
	90%/10%		90P2/10P4

3. Results and Discussion

3.1. Flow Field Structures of the Investigated Droplets

Figure 3 illustrates the cross-section internal flow field in the pure $PODE_2$ droplet and the five investigated binary droplets. As shown in Figure 3a, two opposite radial flows with two symmetrically distributed vortex cores near the droplet surface can be observed in the cross section of the pure $PODE_2$ droplet. This flow field structure has been observed in previous studies of Leidenfrost droplets where the upward vapor flow around the droplet is formed [10,16]. In this work, the high-temperature fuel vapor can be evaporated from the droplet surface by the heating of the flame. The fuel vapor can flow upward along the droplet surface because of the buoyancy effect. This upward vapor flow around the droplet can drive the liquid on the droplet surface to flow upward, which in turn pushes the liquid in the center of the droplet to flow downward. Therefore, the upward vapor flow can induce two opposite radial flows in the cross section of the droplet. As shown in Figure 3a, the flow field structure exhibits two perfect opposite radial flows, which indicates that the convective flow in the pure $PODE_2$ droplet is mainly induced by the surrounding vapor flow.

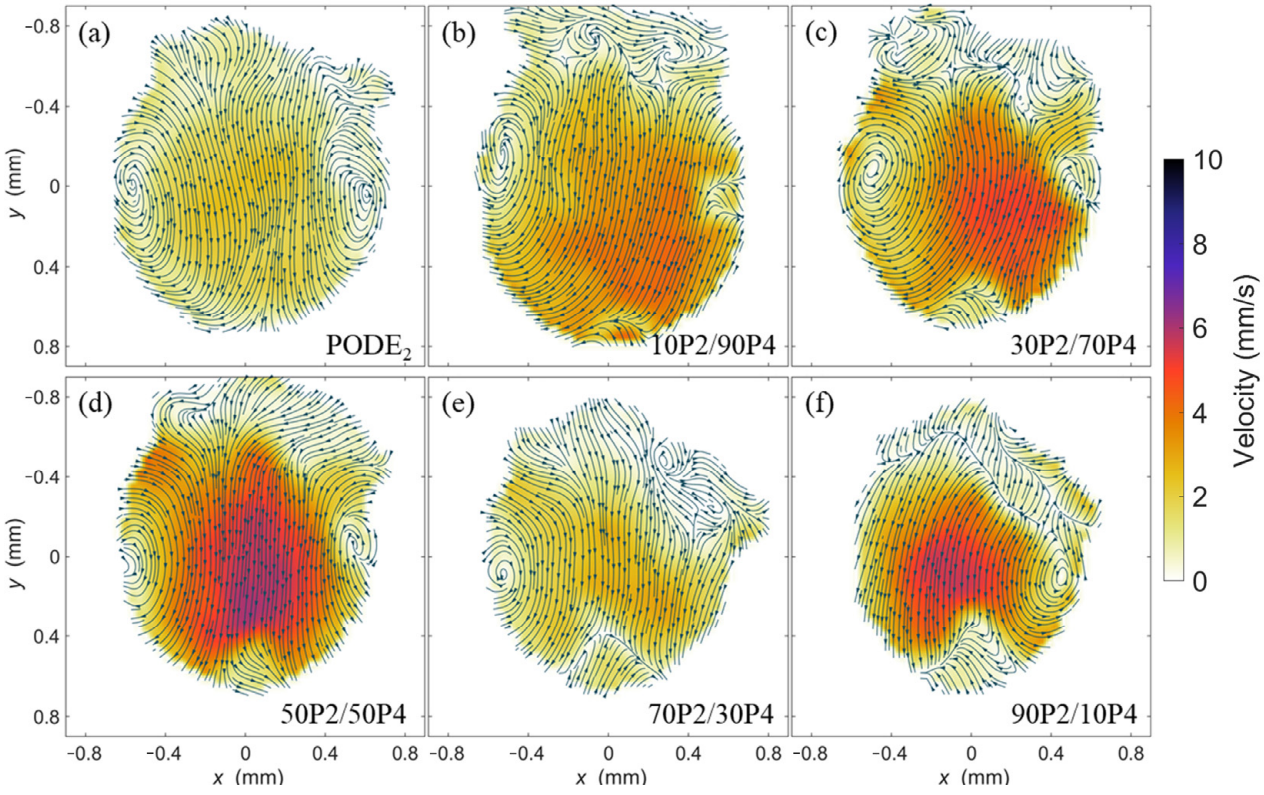


Figure 3. Flow fields in (**a**) the pure $PODE_2$ droplet and (**b**–**f**) the five investigated binary droplets at the middle of the stable evaporation stage during combustion.

For the $PODE_2$/$PODE_4$ droplets, as shown in Figure 3b–f, their main internal flow field structures are generally like the pure $PODE_2$ droplet. However, the radial flows and vortex cores are less symmetric and stable, while sometimes one of the vortices even disappears. For example, as shown in Figure 3b,c,e, the radial flow on the right side disappears and only one vortex core exists and is located near the left side of the droplet surface, while for the 90P2/10P4 droplet in Figure 3f, the situation is contrary. It should be noted that the disappearance of the vortex is quite random; that is, for each binary droplet both left and right vortices may disappear in repeated experiments. Nevertheless, these results reveal that the two opposite radial flows induced by the upward vapor flow around the droplet surface can be disturbed in the binary droplets. Detailed analysis of these phenomena is given in the following two paragraphs.

Unlike the pure droplets, the components in binary droplets are not uniformly distributed because of the preferential evaporation of the highly volatile component on the droplet surface, which can induce the content gradient from the droplet surface to the droplet interior [8]. Due to the different densities and surface tensions of $PODE_2$ and $PODE_4$, the content gradient can lead to the density gradient and surface tension gradient in the binary droplets. Therefore, the convective flow in the binary droplets is not only driven by the surrounding vapor flow but also influenced by the gravitational effect induced by the density gradient [15] and the Marangoni effect induced by the surface tension gradient [12]. For the gravitational effect, the liquid on the droplet surface with higher content of $PODE_4$ (1.06 g/mL in density [20]) tends to flow downward, while the liquid inside the droplet with higher content of $PODE_2$ (0.96 g/mL in density [20]) tends to flow upward. As a result, the gravitational effect can also induce two opposite radial flows in the cross section of the droplet, which were also observed in sessile droplet evaporation by Edwards et al. [14]. It should be mentioned that the radial flows induced by the gravitational effect have opposite directions to the main radial flows induced by the upward vapor flow, which can disturb the main flows.

Under the Marangoni effect, the liquid tends to move toward positions with higher surface tension and temperature [22]. Since the surface tension of $PODE_4$ (30.7 mN/m [20]) is higher than that of the $PODE_2$ (~25 mN/m [20]), the solutal Marangoni effect can drive the liquid flow toward positions with higher content of $PODE_4$. This effect consequently induces the solutal Marangoni flow from the droplet interior to the droplet surface, which has a different disturbance effect to the main flows from the gravitational effect. On the other hand, a temperature gradient also exists on the droplet surface since the supporting fiber heated by the flame can raise the nearby surface temperature. Thus, the thermal Marangoni effect can induce the thermal Marangoni flow from the top of the droplet to the bottom along the droplet surface, which has a similar disturbance effect to the gravitational effect. According to previous studies, the flow velocities caused by the gravitational effect and Marangoni effect are relatively small, at the scale of μm/s [14,15] while the flow velocities caused by the upward vapor flow can be at the scale of cm/s [10,16]. Therefore, the main flow field structures of the investigated binary droplets are still controlled by the upward vapor flow, while local flow field structures at certain regions are disturbed slightly by the gravitational effect and Marangoni effect, which result in the discrepancies of vortices in the binary droplets.

3.2. Flow Velocity Evolution and Distribution of the Investigated Droplets

3.2.1. Spatially Averaged Flow Velocity Evolution of the Investigated Droplets

The blue curves in Figure 4 show the spatially averaged flow velocity evolution of the five investigated binary droplets. It can be seen that there is a short vibration and increase in the averaged flow velocity after ignition. This is mainly because the electric spark in the ignition process can cause a vibration in the droplet and increase the flow velocity. This disturbance in the flow field quickly disappears after around 60 ms, and the droplets enter into the stable evaporation stage when the flow field keeps stable. After a certain period of time, the velocity quickly increases, and the curve becomes unstable. This means that

the droplet has entered into the atomization stage when bubbles are formed and grow in the droplet because of the content gradient and temperature gradient [23]. The droplet atomization process can lead to strong vibration of the droplet, and thus, the averaged flow velocity in the droplet at this stage is relatively large and fluctuant. Therefore, these velocity curves can reveal the atomization delay time of these binary droplets. It can be seen that the 50P2/50P4 droplet has the shortest atomization delay time, which is in accordance with our previous study on the combustion of $PODE_n$ binary droplets [7].

The red points in Figure 4 represent the correlation values of these velocities. According to the DaVis 8.4 software, the velocity can be regarded as accurate if the correlation value is higher than 0.7. Therefore, it can be seen that the velocities at the atomization stage are not accurate because the correlation values are all lower than 0.6. This is mainly because under the strong vibration and large averaged flow velocity conditions, the same particle in the adjacent frames cannot be accurately identified, so the calculation is not reliable. Therefore, only the velocity results in the stable evaporation stage are useful and will be discussed here.

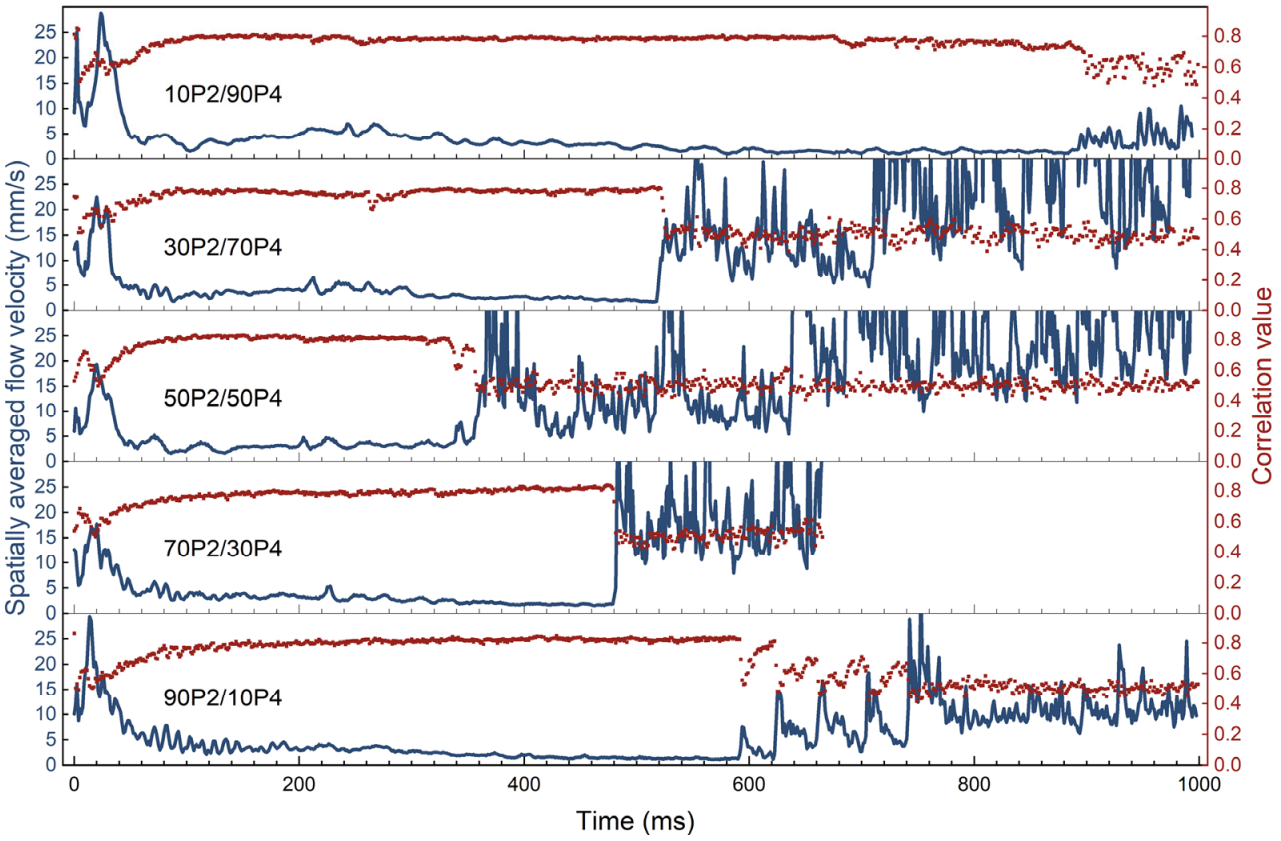


Figure 4. Evolution of the spatially averaged velocities (blue curves) and the corresponding correlation values of the flow velocities (red points) in the five investigated binary droplets.

Figure 5 shows the comparison of spatially averaged flow velocity evolution at the stable evaporation stage among the investigated pure and binary droplets. It can be seen that the binary droplets generally have comparable averaged flow velocities with the pure droplets. For pure droplets, $PODE_2$ and $PODE_4$ droplets generally have comparable flow velocities of around 3 mm/s. Their velocities are relatively stable and stay almost unchanged during the whole droplet evaporation stage. Since the internal flows in the pure droplets are only controlled by the upward vapor flow, it can be seen that the flow velocities caused by the upward vapor flow in the suspended droplets are at mm/s scale. For binary droplets, the content ratios of $PODE_2$ and $PODE_4$ seem to only have little effect on the flow velocity. This is mainly because the content-gradient-induced flow velocities under the

gravitational and Marangoni effect are only at the scale of μm/s [14,15], much smaller than the vapor-flow-induced flow velocities. Therefore, the different content gradients caused by different content ratios of the binary droplets cause little difference to the flow velocity. However, strong fluctuation can be found on the velocity curves of the binary droplets, and their averaged flow velocities first increase a little after ignition and then gradually decrease until atomization. As mentioned above, the flow field in the pure droplet is only controlled by the upward vapor flow, while the flow field in the binary droplet is disturbed by the gravitational effect and Marangoni effect caused by content gradient and temperature gradient. Therefore, the more fluctuant flow velocities in the binary droplets are probably caused by the interaction of these effects, indicating the influence of a multi-component effect on the droplet flow field.

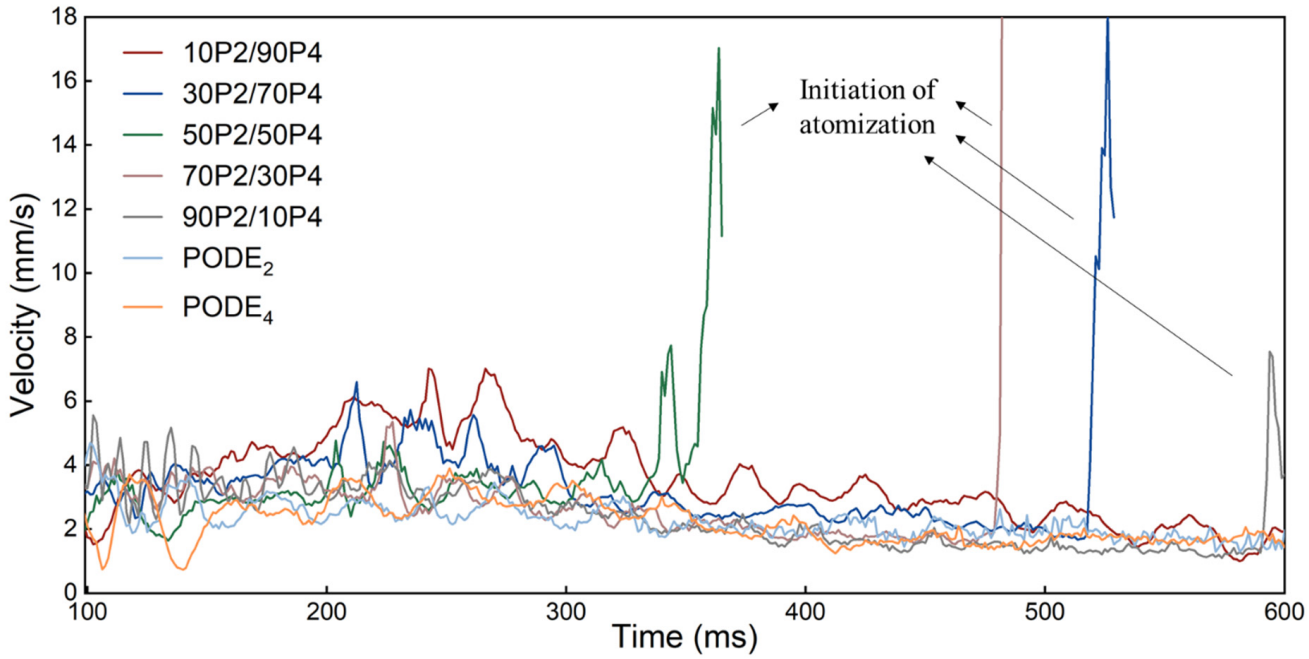


Figure 5. Comparison of the spatially averaged flow velocities at the stable evaporation stage of the investigated pure and binary droplets.

3.2.2. Velocity Distributions of the Investigated Binary Droplets

Figure 6 shows the velocity fields in the five investigated binary droplets at four moments of the stable evaporation stage. It can be seen that the maximum flow velocities are generally located in the droplet interior, while the minimum flow velocities are generally located near the droplet surface. This is mainly because the vortex cores in the binary droplets are formed near the droplet surface, as can be seen in Figure 3. The flow field structures in the studied different binary droplets are generally unstable, so there exists fluctuation of the flow velocities. Figure 7 shows the corresponding vorticity fields in the five investigated binary droplets at the same four moments of the stable evaporation stage. It can be seen that the maximum vorticities are generally located near the droplet surface, while the minimum vorticities are generally located in the droplet interior, which is opposite to the trend of velocity fields. For the 50P2/50P4 binary droplet, the atomization delay time is the smallest. Therefore, the velocity field and vorticity field of the 50P2/50P4 binary droplet in Figures 6 and 7 at $t = 500$ ms are missing because the binary droplet has already entered into the atomization stage.

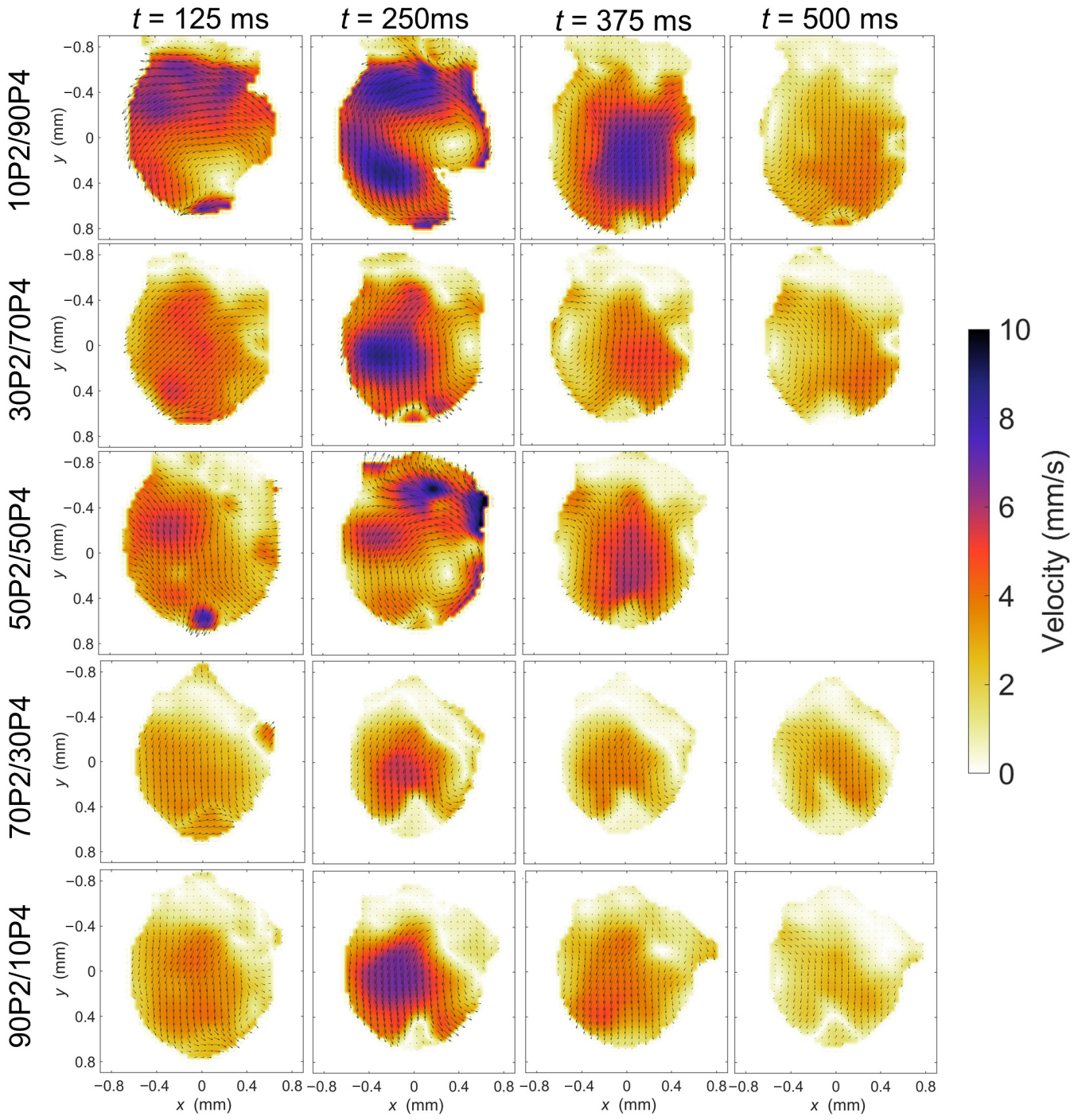


Figure 6. Velocity fields in the five investigated binary droplets at four moments (125, 250, 375, and 500 ms) of the stable evaporation stage.

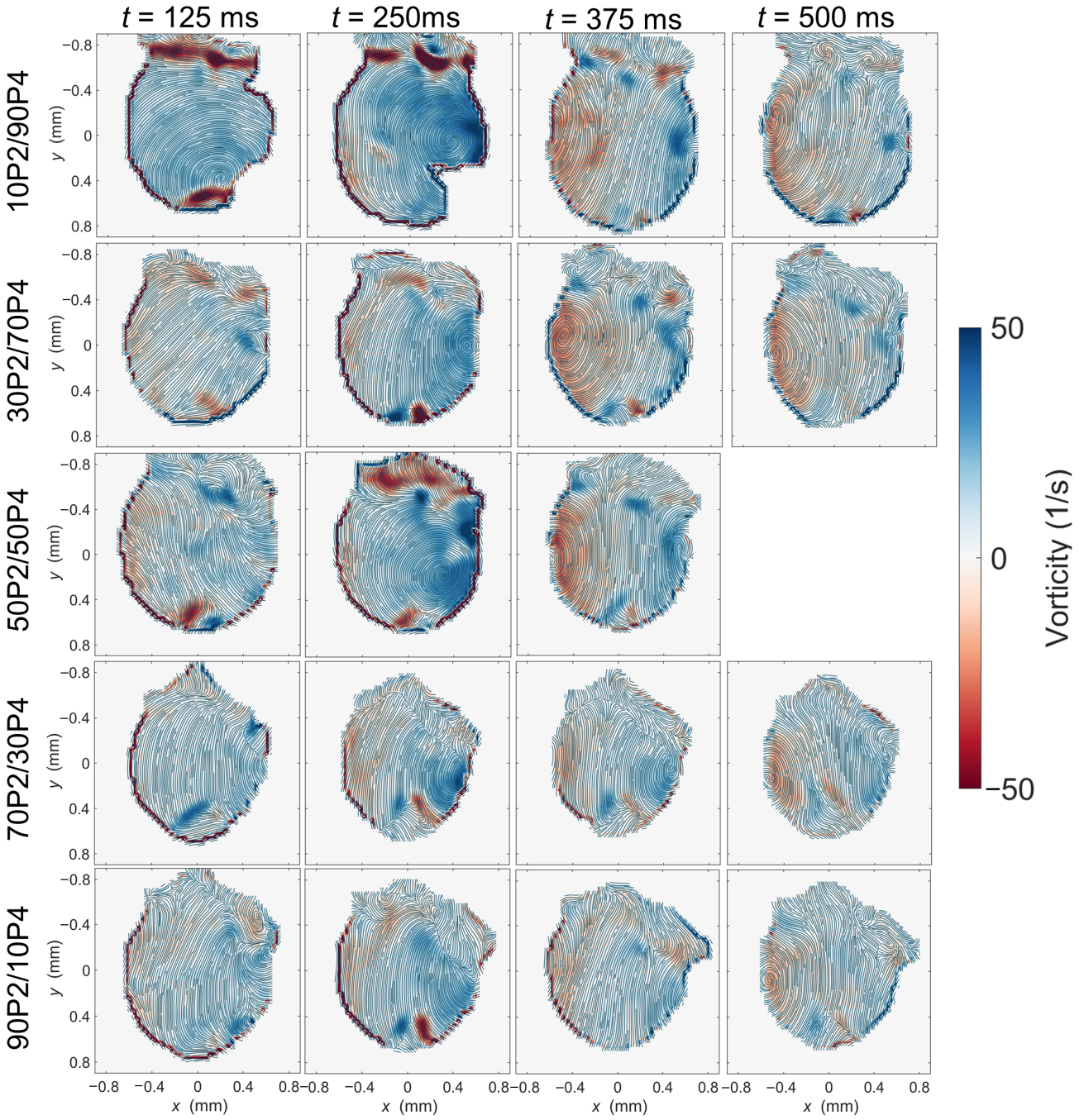


Figure 7. Vorticity fields in the five investigated binary droplets at four moments (125, 250, 375, and 500 ms) of the stable evaporation stage.

Figure 8 shows the corresponding velocity profiles of the five investigated binary droplets along the droplet horizontal radial direction at four moments of the stable evaporation stage. The velocities at r/R_d close to ± 1 are not presented as this region is very close to the droplet surface and out of the effective data region. The velocity profiles mainly peak in the droplet interior, while the local minima represent the vortex cores formed by the radial flows. The main body of a velocity profile generally has a parabolic shape, except for those at $t = 125$ ms (the shortest moment after ignition in Figure 8). The weak parabolic shapes or even plain shapes at $t = 125$ ms are probably due to the vortex structures in the droplets still not being formed and the flow velocity not showing superiority in the droplet interior. It can be observed from Figure 8 that for each binary droplet, the peak velocity

first increases from $t = 125$ ms to $t = 250$ ms to a value of 5–9 mm/s as the radial flows and vortex structures are formed. Then, the peak velocity gradually decreases to a value of around 3 mm/s from $t = 250$ ms to $t = 500$ ms as the droplet approaches the atomization stage, which is in accordance with the findings in previous work [16]. From 125 ms to 500 ms, the evolution of the velocity is fluctuant for each of the binary droplets because of the disturbance in the flow field. The velocities of these binary droplets are all at the same magnitude, and their differences are small.

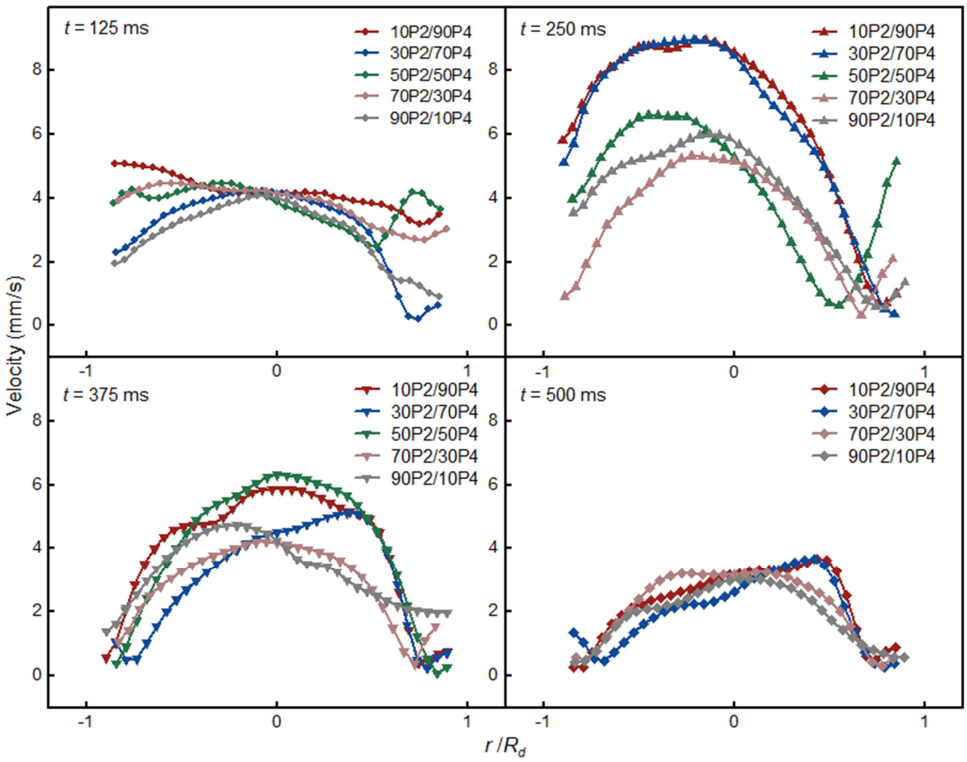


Figure 8. Velocity profiles of the five investigated binary droplets along the droplet horizontal radial direction at four moments (125, 250, 375, and 500 ms) of the stable evaporation stage. The horizontal coordinate denotes the radial distance from the droplet center normalized by the droplet radius, while the vertical coordinate represents the flow velocity at the corresponding position.

In this work, it should be mentioned that the investigated binary droplets can all undergo the atomization process. This observation implies that although the internal flow in the binary droplets can enhance the mass transfer process and affect the content gradient, the influence is not strong enough to break the content gradient in the droplet. Actually, the averaged flow velocities (V_{aver}) in the five investigated binary droplets are only around 3 mm/s, as shown in Figure 5, which is a rather small value compared with the flow velocities in the Leidenfrost droplets, which are generally at the magnitude of 10 cm/s [10,16]. Supposing that the averaged droplet diameter (D_{aver}) at the stable evaporation stage is:

$$D_{aver} = (D_0 + D_1)/2 \quad (1)$$

where D_0 is the initial droplet diameter, and D_1 is the final droplet diameter of the stable evaporation stage, the averaged perimeter of the radial flow (L) approximately equals to half of the droplet perimeter (C) plus the averaged droplet diameter.

$$L = C/2 + D_{aver} = (\pi/2 + 1)\, D_{aver} \quad (2)$$

For each binary droplet, the approximate radial flow laps n at the measured duration time of the stable evaporation stage (t_1) can be calculated with Equation (3).

$$n = V_{\text{aver}} t_1 / L \tag{3}$$

where V_{aver} is approximated as 3 mm/s. As shown in Table 2, at the whole stable evaporation stage, the radial flows can only run about one lap at the most, which implies that the convection-induced mass transfer is relatively weak, and consequently, the content gradient along the radial direction of the droplets is still controlled by mass diffusion.

Table 2. A list of droplet diameter parameters (D_0, D_1, and D_{aver}), measured duration time t_1, averaged maximum perimeter of the radial flow L, and radial flow laps n of the five investigated binary droplets at the stable evaporation stage.

Binary Droplet	D_0 (mm)	D_1 (mm)	D_{aver} (mm)	t_1 (ms)	L (mm)	n
10P2/90P4	1.270	0.680	0.975	852	2.506	1.020
30P2/70P4	1.360	0.910	1.135	465	2.917	0.478
50P2/50P4	1.280	1.100	1.190	280	3.058	0.275
70P2/30P4	1.540	1.230	1.385	443	3.669	0.373
90P2/10P4	1.430	1.070	1.250	495	3.212	0.462

4. Conclusions

This work uses Micro-PIV to investigate the internal flow fields in the $PODE_2/PODE_4$ binary droplets with different content ratios during combustion, as well as those of pure $PODE_2$ and $PODE_4$ droplets for comparison. The flow field structure, flow velocity, and the influence of the internal flow on the mass transfer process and content gradient formation in the binary droplets are analyzed. The main conclusions are summarized below:

(1) The buoyancy-driven upward vapor flow around the droplet is found to initiate two opposite radial flows in the droplet that form two vortex cores near the surface, while the gravitational effect and Marangoni effect resulting from the content and temperature gradients in the binary droplets can induce disturbance to the two flows.
(2) The binary droplets have comparable spatially averaged flow velocities at the stable evaporation stage to those of pure droplets, which are around 3 mm/s. The velocity curves of the binary droplets are more fluctuant and tend to slightly increase and reach peak values at around 250 ms, and then decrease until droplet atomization.
(3) The flow velocities in the droplet interior are generally higher than those near the droplet surface, forming a parabolic velocity profile along the horizontal radial direction. The peak velocity first increases to 5–9 mm/s as the radial flow and vortex structure start to form and then decreases to around 3 mm/s until droplet atomization.
(4) The radial flow with a spatially averaged velocity of 3 mm/s can only run around one lap at the most during the stable evaporation, which implies that the convection-induced mass transfer is relatively weak, and consequently, the content gradient along the radial direction of the binary droplet is still mainly controlled by mass diffusion.

Author Contributions: B.H.; data curation, formal analysis, investigation, and writing—original draft, H.Z.; investigation, methodology, software, Z.L.; methodology, X.Y.; methodology, W.L.; methodology, Y.L.; conceptualization, resources, supervision, writing—review and editing. All authors have read and agreed to the published version of the manuscript.

Funding: This research was funded by the National Natural Science Foundation of China (52206164), Science Center for Gas Turbine Project (P2022-B-II-017-001), Oceanic Interdisciplinary Program of Shanghai Jiao Tong University (SL2022ZD104), and China Postdoctoral Science Foundation (2021M702098).

Institutional Review Board Statement: Not applicable.

Informed Consent Statement: Not applicable.

Data Availability Statement: Data will be made available on request.

Acknowledgments: The authors appreciate Xiaoxiang Shi and Yi Zhang for the constructive discussion.

Conflicts of Interest: The authors declare no conflict of interest.

References

1. Pham, Q.; Park, S.; Agarwal, A.K.; Park, S. Review of Dual-Fuel Combustion in the Compression-Ignition Engine: Spray, Combustion, and Emission. *Energy* **2022**, *250*, 123778. [CrossRef]
2. Alhajj, N.; O'Reilly, N.J.; Cathcart, H. Leucine as an Excipient in Spray Dried Powder for Inhalation. *Drug Discov. Today* **2021**, *26*, 2384–2396. [CrossRef] [PubMed]
3. Brutin, D.; Sobac, B.; Loquet, B.; Sampol, J. Pattern Formation in Drying Drops of Blood. *J. Fluid Mech.* **2011**, *667*, 85–95. [CrossRef]
4. Deegan, R.D.; Bakajin, O.; Dupont, T.F.; Huber, G.; Nagel, S.R.; Witten, T.A. Capillary Flow as the Cause of Ring Stains from Dried Liquid Drops. *Nature* **1997**, *389*, 827–829. [CrossRef]
5. Wu, L.; Zhou, Z.; Zhang, X.; Liu, Y.; Wang, G.; Zhang, K. Characterization of Microstructure and Passive Film Difference of FeCrMoCB Amorphous Coatings Affected by Feedstock Specific Surface Area. *Surf. Coat. Technol.* **2023**, *457*, 129333. [CrossRef]
6. Park, J.; Moon, J. Control of Colloidal Particle Deposit Patterns within Picoliter Droplets Ejected by Ink-Jet Printing. *Langmuir* **2006**, *22*, 3506–3513. [CrossRef] [PubMed]
7. Huang, B.; Yang, X.; Zhang, Y.; Zhang, H.; Li, W.; Li, Y. Characterizing Combustion and Atomization of PODEn and Ethanol/PODEn Binary Droplets. *Fuel* **2023**, *341*, 127672. [CrossRef]
8. Law, C.K. Internal Boiling and Superheating in Vaporizing Multicomponent Droplets. *AIChE J.* **1978**, *24*, 626–632. [CrossRef]
9. Law, C.K. Multicomponent Droplet Combustion with Rapid Internal Mixing. *Combust. Flame* **1976**, *26*, 219–233. [CrossRef]
10. Bouillant, A.; Mouterde, T.; Bourrianne, P.; Lagarde, A.; Clanet, C.; Quéré, D. Leidenfrost Wheels. *Nat. Phys.* **2018**, *14*, 1188–1192. [CrossRef]
11. Christy, J.R.E.; Hamamoto, Y.; Sefiane, K. Flow Transition within an Evaporating Binary Mixture Sessile Drop. *Phys. Rev. Lett.* **2011**, *106*, 205701. [CrossRef] [PubMed]
12. Diddens, C.; Li, Y.; Lohse, D. Competing Marangoni and Rayleigh Convection in Evaporating Binary Droplets. *J. Fluid Mech.* **2021**, *914*, A23. [CrossRef]
13. Diddens, C.; Tan, H.; Lv, P.; Versluis, M.; Kuerten, J.G.M.; Zhang, X.; Lohse, D. Evaporating Pure, Binary and Ternary Droplets: Thermal Effects and Axial Symmetry Breaking. *J. Fluid Mech.* **2017**, *823*, 470–497. [CrossRef]
14. Edwards, A.M.J.; Atkinson, P.S.; Cheung, C.S.; Liang, H.; Fairhurst, D.J.; Ouali, F.F. Density-Driven Flows in Evaporating Binary Liquid Droplets. *Phys. Rev. Lett.* **2018**, *121*, 184501. [CrossRef] [PubMed]
15. Li, Y.; Diddens, C.; Lv, P.; Wijshoff, H.; Versluis, M.; Lohse, D. Gravitational Effect in Evaporating Binary Microdroplets. *Phys. Rev. Lett.* **2019**, *122*, 114501. [CrossRef] [PubMed]
16. Lyu, S.; Tan, H.; Wakata, Y.; Yang, X.; Law, C.K.; Lohse, D.; Sun, C. On Explosive Boiling of a Multicomponent Leidenfrost Drop. *Proc. Natl. Acad. Sci. USA* **2021**, *118*, e2016107118. [CrossRef] [PubMed]
17. Antonov, D.V.; Kuznetsov, G.V.; Misyura, S.Y.; Strizhak, P.A. Temperature and Convection Velocities in Two-Component Liquid Droplet until Micro-Explosion. *Exp. Therm. Fluid Sci.* **2019**, *109*, 109862. [CrossRef]
18. He, M.; Piao, Y. An Experimental Study on the Phenomena inside the Burning Aviation Kerosene Droplet. *J. Therm. Sci.* **2021**, *30*, 2202–2213. [CrossRef]
19. Mandal, D.K.; Bakshi, S. Evidence of Oscillatory Convection inside an Evaporating Multicomponent Droplet in a Closed Chamber. *J. Colloid Interface Sci.* **2012**, *378*, 260–262. [CrossRef]
20. Awad, O.I.; Ma, X.; Kamil, M.; Ali, O.M.; Ma, Y.; Shuai, S. Overview of Polyoxymethylene Dimethyl Ether Additive as an Eco-Friendly Fuel for an Internal Combustion Engine: Current Application and Environmental Impacts. *Sci. Total Environ.* **2020**, *715*, 136849. [CrossRef]
21. Wieneke, B. PIV Uncertainty Quantification from Correlation Statistics. *Meas. Sci. Technol.* **2015**, *26*, 074002. [CrossRef]
22. Pearson, J.R.A. On Convection Cells Induced by Surface Tension. *J. Fluid Mech.* **1958**, *4*, 489–500. [CrossRef]
23. Rao, D.C.K.; Karmakar, S.; Basu, S. Bubble Dynamics and Atomization Mechanisms in Burning Multi-Component Droplets. *Phys. Fluids* **2018**, *30*, 067101. [CrossRef]

Disclaimer/Publisher's Note: The statements, opinions and data contained in all publications are solely those of the individual author(s) and contributor(s) and not of MDPI and/or the editor(s). MDPI and/or the editor(s) disclaim responsibility for any injury to people or property resulting from any ideas, methods, instructions or products referred to in the content.